A microfluidics-integrated impedance/surface acoustic resonance tandem sensor

Sensing and Bio-Sensing Research 25 (2019) 100291

Contents lists available at ScienceDirect

Sensing and Bio-Sensing Research

journal homepage: www.elsevier.com/locate/sbsr

A microfluidics-integrated impedance/surface acoustic resonance tandem sensor

Kiryl Kustanovich[a], Ventsislav Yantchev[a,b,*], Baharan Ali Doosti[a], Irep Gözen[a,c,d], Aldo Jesorka[a]

[a] Department of Chemistry and Chemical Engineering, Chalmers University of Technology, SE-412 96 Göteborg, Sweden
[b] Q-Arts Consulting EOOD, 3000 Vratsa, Bulgaria
[c] Centre for Molecular Medicine Norway, Faculty of Medicine, University of Oslo, 0318 Oslo, Norway
[d] Department of Chemistry, Faculty of Mathematics and Natural Sciences, University of Oslo, 0315 Oslo, Norway

ARTICLE INFO

Keywords:
Surface acoustic wave
Resonator
Electrochemical impedance spectroscopy
Sensor
Microfluidics
IDE

ABSTRACT

We demonstrate a dual sensor concept for lab-on-a-chip in-liquid sensing through integration of surface acoustic wave resonance (SAR) sensing with electrochemical impedance spectroscopy (EIS) in a single device. In this concept, the EIS is integrated within the building blocks of the SAR sensor, but features a separate electrical port. The two-port sensor was designed, fabricated, and embedded in a soft polymer microfluidic delivery system, and subsequently characterized. The SAR-EIS tandem sensor features low cross-talk between SAR and EIS ports, thus promoting non-interfering gravimetric and impedimetric measurements. The EIS was characterized by means of the modified Randle's cell lumped element model. Four sensitive parameters could be established from the tandem sensor readout, and subsequently employed in a proof of principle study of liposome layers and their interaction with Ca^{2+} ions, leading to transformation into molecular film structures. The associated shift of the sensing quantities is analysed and discussed. The combination of impedimetric and gravimetric sensing quantities provides a unique and detailed description of physicochemical surface phenomena as compared to a single mode sensing routine.

1. Introduction

The integration of in-liquid sensing units in lab-on-a-chip devices is among the key challenges on the road to micro total analysis systems (μTAS) [1]. The combination of various independent sensor principles on the same chip is particularly attractive, but also especially difficult to implement [2]. Lowered fabrication costs, orthogonal and multi-analyte sensing capability, and reduced time of analysis are competing with increased design requirements, interfacing challenges, and additional materials compatibility considerations. Therefore, the combination of two or more complementary sensing principles in a single physical sub-unit is very attractive, as it facilitates interfacing with the fluidic framework, and reduces the required design efforts.

A variety of different individual sensors capable of gas detection, or chemical and biochemical analysis in a liquid environment have been reported in the past, driven by demands by industrial technology manufactures for small inexpensive high-performance sensors [3]. Commonly, these devices are based upon the measurement of resonance frequency shifts in piezoelectric materials, which are related to mass changes at the sensing interface (gravimetric analysis using acoustic wave technology [4–6]), or upon monitoring changes in the electrical impedance response of a system (electrochemical transduction techniques [7]). Intrinsically label-free, the gravimetric and impedimetric sensors require in many cases fewer or no sample preparation steps, compared to sensors that involve light absorption or emission, where the attachment of an optical label is often necessary.

The introduction of acoustic wave technology into lab-on-a-chip platforms was an important milestone on the road to micro total analysis systems, providing not only mass sensing capability and direct electronic readout [8], but also additional sample preparation functions, such as fast fluidic actuation, contact-free particle manipulation and sorting [9]. Moreover, the electrode interfaces of acoustic wave sensors provided opportunities for the simultaneous evaluation of analyte-related electrochemical processes in conjunction with their gravimetric determination. Specifically, electrochemical impedance spectroscopy was implemented along with acoustic wave sensing in combination devices, e.g., integrated with a miniaturized polymeric analyte delivery system for assessing water toxicity [10], studies of molecular lipid films [11], and some other applications [12–16]. In such studies, integrated sensors that detect mass changes and

* Corresponding author at: Department of Chemistry and Chemical Engineering, Chalmers University of Technology, SE-412 96 Göteborg, Sweden.
E-mail address: ventsi.yantchev@gmail.com (V. Yantchev).

https://doi.org/10.1016/j.sbsr.2019.100291
Received 7 April 2019; Received in revised form 12 June 2019; Accepted 2 July 2019

viscoelastic properties, and provide a response related to the dielectric properties of the analyte at the sensor interface, can provide complementary information about both mechanical and electrical characteristics of the chemical or biochemical system under investigation. Simultaneous, complementary measurements are a reliable way to establish the reproducibility of individual sensor data, but can as well reveal additional information of system features and behaviour [10,11,13]. For instance, Briand et al. have performed EIS experiments to study the interaction of the supported lipid bilayer (SLB) with the pore-forming toxin gramicidin D (grD), where no significant change in QCM-D response was observed upon addition of low grD concentrations, due to the small molecular weight of the peptide. However, the change of electrical properties of the SLB upon insertion of active ion channels owed to the presence of grD molecules inside the bilayer was confirmed by the EIS response obtained. For higher concentrations, the QCM-D data showed dramatic changes in the viscoelastic properties of the membrane while the EIS spectra did not change [11]. Moreover, the penetration depth of the fringing electric fields above the planar interdigital electrodes reaches far beyond the acoustic penetration depth, as it is proportional to the spacing between the center lines of the electrode fingers [17]. This opens new possibilities for bioanalytical studies on cells and pathogenic microorganisms, where the biomembrane at the cell-surface interface, and the integrity of the bulk structure can be simultaneously monitored. Examples for either technique applied individually have been reported earlier [18,19]. A combination of pathogen detection and drug response determination could, for example, be an application of the tandem sensor.

Impedance spectroscopy (IS) integration with acoustic wave sensing has been earlier successfully demonstrated with the quartz crystal microbalance (QCM) platform [10,11]. These implementations feature an additional reference electrode, which occupies additional space as it is not functional part of the QCM itself. Furthermore, the comparatively large physical size of the conventional QCM sensor limits miniaturization and sensitive measurements on small surface areas, as well as parallelisation and integration with microfluidic sample platforms.

High frequency alternatives to QCM have also been developed, which allow for sensor area reduction and parallelisation. Significant efforts in the field of microfluidics-integrated sensing technology were focused on thin-film electroacoustic technology (often referred to as piezo-MEMS). Microsystems based on this approach have a particularly strong potential for commercialization, due to fabrication technologies established by the radio frequency (RF) filter industry. Thickness-excited quasi-shear film bulk acoustic resonators (shear-FBARs) [20,21] have shown the strongest potential so far, since they have reached the stage of commercial sensing array prototypes [22,23]. Thin-film S0-Lamb waves and their equivalent extensional plate modes are also promising [24,25]. However, these approaches are limited by practical considerations concerning fabrication process uniformity, device fragility and strong local pressure sensitivity. The latter two being inherent for all thin-film membrane devices.

Alternatively, shear surface transverse acoustic waves (SH-SAW) [26] have been explored as a high-frequency alternative to QCM. The high frequency of operation is associated with smaller sensor dimensions, because the acoustic wavelength scales inversely proportional with the operation frequency. Typically, SAW sensor implementations rely on delay-line configurations where the SAW propagates through a comparatively long distance between input and output transducers (two-port configuration) to accumulate sufficient time delay and phase shift. Thus, the frequency scaling effects are to a large extent compensated. As a result, SAW delay line sensors are relatively large and characterized by strong transmission loss when operated in-liquid, so that additional signal processing is often required to remove interferences. These limitations can be overcome by utilizing a two-port SAW resonator with smaller distance between the transducers and a set of reflectors on each end [27–29]. However, the SAW transducers in this configuration remain susceptible to liquid conductivity and can become short-circuited. To protect the transducers from the liquid environment, and to confine the analyte in the sensing area, SH-SAW sensors were integrated with PDMS microchannel system at the expense increased damping losses [30]. Alternatively, sensing of biomolecules was reported in a dry state after removal of the liquid from the sensor, employing Rayleigh SAW two-port resonators. This eliminates the interdigital transducer (IDT) interaction with conductive liquids [31]. Moreover, the two-port configuration is somewhat problematic when parallelization needs to be considered. For that reason, one-port SAW sensor configurations have been developed as a high frequency and small form-factor alternative to the QCM [32].

We have recently introduced a microfluidics-integrated high frequency sensor concept, combining the advantages of the 1-port measurement setup with wafer-scale, commercially viable fabrication processes and materials. This concept of separate driving and sensing units was for the first time implemented in SAW sensor technology [33,34]. Our device utilizes the reflective gratings of a one-port SAW resonator as mass loading-sensing elements, with the SAW IDT being protected from the measurement environment and acting only as a read-out element. The optimum sensor performance has been derived from a trade-off between the ability of the IDT to probe the sensing blocks and their sensitivity determined by the amount of energy confinement [35]. This configuration achieves low susceptibility to damping with good control over device impedance, reduces the complexity of the readout electronics, and facilitates the integration in sensor arrays. The new surface acoustic resonance (SAR) sensor can detect mass and viscous loadings in liquid at a level comparable and better to the state-of-art high frequency gravimetric sensors, while also demonstrating lower damping from viscous loading. Our concept provided significant practical advantages for typical sensor integration and deployment, such as the ability to sense in conductive and highly viscous media.

In the current work we demonstrate the integration of both the SAW gravimetric and electrochemical impedance spectroscopy (EIS) sensing concepts in a single device with microfluidic support. Unlike other functional combinations, here the EIS is integrated within one of the SAW sensor building blocks with a separate EIS interface port. We gain the ability to simultaneously record impedimetric and gravimetric data for chemical and biochemical analytes, while enabling high sensor parallelisation. The envisaged utility of this sensing combination can be considered in two aspects. On one hand, impedimetric data would allow for precise calibration of the experiments, while on the other hand can be used complementary to the gravimetric data to improve the sensing specificity and gain additional information about dielectric properties of the analyte deposits on the surface. The tandem of impedimetric and gravimetric patterns can represent a unique signature for a given analytical system.

The demonstrated integration relies on the one-port SAR sensor design specifically employing the SAW reflector gratings as sensing elements, spatially separated from the IDT read-out. Thus, the SAW reflective gratings, which usually are electrically short-circuited, can be reconfigured into an interdigitated electrode (IDE) capacitive configuration, galvanically isolated from the SAW transducer. In addition to the galvanic isolation, SAW and impedimetric measurements are performed within noninterfering frequency bands leading to significantly suppressed measurement crosstalk. Impedance spectroscopy is performed at frequencies below 1 MHz, while SAW resonance is monitored at about 185 MHz. It is also noted that in impedance spectroscopy integration with QCM, the sensing system employs relatively close (i.e. eventually interfering) frequency bands as the QCM is usually operating in the 5 MHz–10 MHz frequency range.

The integrated SAR-impedance spectroscopy dual-sensing device was tested in an aqueous environment in the presence of lipid reservoir deposits on the sensor surface, which was further subjected to interaction with Ca^{2+} ions. When lipid vesicles attach and spread on the sensor surface, the acoustic wave detects changes in mass and viscoelasticity by detecting shifts in resonant frequency and the magnitude of

the conductance peak of the SAR sensor. The integrated EIS provides information about the electrical properties of the lipid membrane, such as its dielectric permittivity and dielectric loss (resistivity).

Lipid membranes are specifically chosen as a versatile model system for mimicking the plasma membranes of biological cells. They are utilized for membrane protein investigations, studies of cell adhesion, membrane fusion and interaction with various molecules [36,37]. We consider these nanometre-thick membranes particularly suitable for practically evaluating sensor performance, as they provided small mass loadings and electrical perturbations, ease of deposition on a solid support, and a rich feature set of electrical and mechanical properties that strongly depend on the composition and the chemical environment.

2. Sensor design and measurement configuration

2.1. Design

The principles of operation and the fabrication technology of the one-port SH-SAW resonant sensor have been thoroughly discussed in previous work [34,35]. Here we describe the sensor structure in brief, and emphasize its integration with impedance spectroscopy (IS).

Fig. 1 shows a PDMS mould containing the microfluidic circuits to be interfaced with the reflector gratings, and an air cavity to be positioned above the IDT. It is separately fabricated and bonded onto the die containing the planar one-port sensor structure. In the original design, the electrically short-circuited reflective gratings are used as sensing elements, with the microfluidic structures placed on top, while the wideband IDT is protected from the measurement environment by an air cavity. The resonant frequency shifts are determined primarily by the mass load deposited over the reflector grating, which perturbates the propagation properties (phase velocity and reflectivity) of the acoustic wave travelling under it. We use *Y*-cut $LiNbO_3$ as piezoelectric substrate. This material is known for its high electromechanical coupling coefficient of about 25% for Leaky SAW (LSAW) that propagates with bulk radiation losses along the crystal *X* axis [38]. The "leaky" nature of the wave is suppressed by means of an Au periodic strip grating that slows down the wave, converting it to a surface-guided SH-SAW while efficiently reflecting it back to the resonator [39]. Alternatively, the recently introduced hetero-acoustic layer substrates employing $LiTaO_3$ layer on Quartz can be employed, since they offer reasonably high electromechanical coupling and temperature stability [40].

The integration of the one-port SAW sensor with impedance spectroscopy is embodied through changes in the electrical connections of the strips in one or both of the SAW reflector gratings. In this new configuration one of the grating busbars remains a common ground to the IDT, while the other becomes an EIS signal pad. The grating strips are now connected as interdigitated electrodes. Forming a regular IDE with periodicity of the polarity resembling that of the IDT (2 strips per λ, where λ is the SAW wavelength at resonance) should be avoided, since such structure will receive the propagating SH-SAWs electrically, and causes re-excitation of SAWs because of electrical impedance mismatch at the IDE ports. That will ultimately perturb the SAW sensitivity due to externally induced wave interference effects. Instead, the IDE should be interdigitated in split electrode configuration [41], with the frequency of SAW excitation being different from the SAW resonance frequency. Thus, effects of SAW re-excitation and SAW related charge accumulation are readily avoided at the cost of reduced static capacitance of the structure.

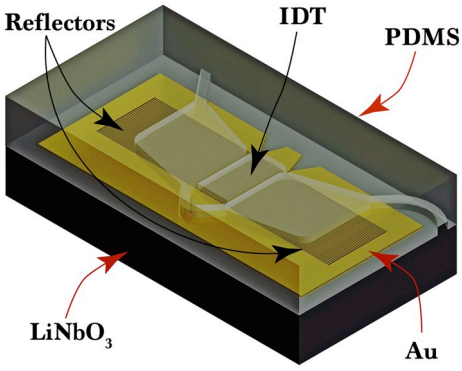

Fig. 1. 3D-rendered image of the SAW sensor. The sensor utilizes a Y-cut $LiNbO_3$ substrate with Au strip gratings, which form the IDT and reflectors in a resonant topology. A PDMS microfluidic analyte delivery system is bonded on top of a one-port SAW resonator.

Here we propose a trade-off IDE design with retained capacitance, employing a split configuration of 3 electrodes per λ in the first 10λ next to the IDT, while the rest is in regular IDE configuration with 2 strips per λ. In such a configuration the SAW energy is strongly confined near the IDT, while attenuating along the reflectors. This attenuation is further boosted by the damping effects in the presence of liquid in the microfluidic containers. Accordingly, SAW regeneration is not likely to appear in the regular IDE part. It is noted that SAW regeneration is associated with the formation of charges on the strips that are in synchronicity with the SAW at resonance. Thus, the split-electrode section of the IDE can ensure cancelling of the SAW induced charge, and provide sufficient isolation between the EIS and the IDT ports. Furthermore, the IDE structure was reduced to only one of the reflector gratings, while the other remained electrically grounded. The latter was needed in view of ensuring easy contacting to the SAW and EIS ports.

In Fig. 2, a sketch view of the implemented design is shown along with image of the SAW-EIS sensing chip as fabricated. The contact pads are fabricated long enough to be able to be contacted outside the PDMS microfluidic device. We currently develop a much more robust test fixture enabling chip size reduction and automated measurements, which employs spring-loaded contacts applied directly through the PDMS mould to the SAW and EIS ports, thus avoiding the use of long contact pads which introduce some parasitic resistance and capacitive crosstalk between the ports.

The integrated SAR-EIS sensor occupies a very small area in the range of 2 mm^2 (Fig. 2b), while the microfluidic inlets and assembly procedures require chip dimensions in the range of 1 cm^2. Accordingly, a minimal integration of about 5 SAR-EIS sensors within the same microfluidic chip with additional inlets is feasible, enabling the design of sensor array systems within an area comparable to the space occupied by a single QCM sensor. Parallelisation of sensors makes simultaneous measurement of several analytes in the same sample possible, or parallel measurements of the same analyte for improved reliability.

Details of the fabricated SAW-EIS sensor are shown in Fig. 3.

2.1.1. Device fabrication

A detailed description of the fabrication process has been provided in earlier publications [34]. Briefly, the metallization on top of a *Y*-cut $LiNbO_3$ substrate consists of a 25 nm Ti adhesion layer, a 260 nm Au functional layer, and a 15 nm Ti cap layer. A 100 nm thick SiO_2 passivation layer is deposited on top of the device to protect the electrodes from corrosion, and to increase bonding strength with the PDMS microfluidic delivery system. In view of the EIS performance, the additional coating with a dielectric film such as SiO_2 is also known to further suppress the Faradaic response of the system [42]. Both the IDT and the reflectors are formed by a periodic grating array with 10 μm pitch (p_0), and a strip width of about $p_0/2$. The entire stack is 300 nm thick, and the device aperture is $W = 40p_0$. The IDT consists of 7 pairs of electrodes for wideband operation with a wavelength at synchronism $\lambda = 2p_0 = 20$ μm. The number of strips in each reflector is 69, of which 49 overlap with a microfluidic container. A variation of grating reflectivity is introduced by means of narrowing the local mark-to-pitch

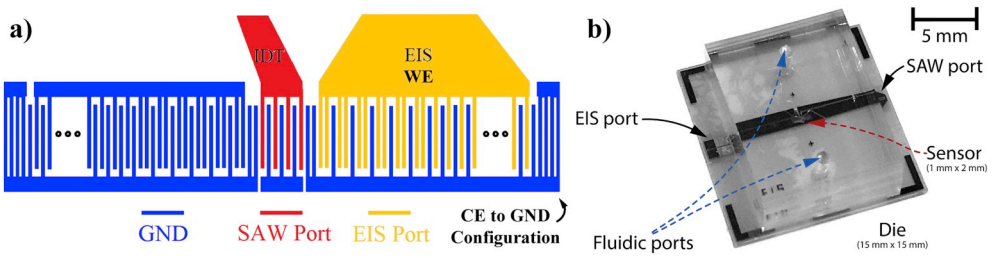

Fig. 2. a) Sketch view of the implemented design (WE stands for work electrode, CE for counter electrode, GND is a ground) and b) photograph of the SAR/EIS tandem sensor integrated with microfluidic device. The sensor contact pads (left and right sides) are appropriately sized for interfacing with contact measurement probes.

ratio of each reflector near the IDT in order to confine a larger amount of SAW energy in the microfluidic containers, and thus to enhance the device gravimetric sensitivity. We referred to this design enhancement as lateral energy confinement [35].

The 1 cm thick polydimethylsiloxane (PDMS) microfluidic analyte and solution delivery system (channel width × height: 50 µm × 50 µm) was fabricated using standard soft lithography [43,44], and O_2-plasma-bonded onto the surface of the one-port SAW resonator.

2.1.2. Measurements

The crosstalk between the sensing ports was initially tested by measuring the transmission insertion loss between the two ports. The S_{21} measurement was performed by means of a vector network analyser (VNA) in the frequency range 300 kHz–200 MHz, limited by the lowest frequency of the VNA (Planar 304/1, Copper Mountain Technologies, USA). The transmission loss between the IDT and the EIS port measured near 185 MHz (the SAW resonance frequency) was found to be as low as −60 dB, while in the range from 300 kHz to 1 MHz it was varying from −120 dB to −90 dB. This crosstalk is purely capacitive and is introduced by the contact pads. An improvement through optimized interfacing can be anticipated. It is further noted that the EIS operates at a frequency where acoustic waves are not excited, thus both functionalities, i.e. acoustic sensing and EIS sensing, can be operated independently. Our initial tests of the sensor ports in liquid environment have shown practically no mutual interference and influence on the measurement data. The noise of the resonance frequency measurement was below 0.5 ppm, which establishes the limit of acoustics frequency detection. This noise number is typical for the VNA-supported measurements of the SAW resonance frequency [35].

Fig. 4 shows the measurement setup. The sensor is mounted on a temperature control stage with 0.1 K temperature stability [35]. It allows for simultaneous measurement of the SAW and the EIS response. For that purpose, the IDT is probed by a VNA with a set of measurement probes (Picoprobe, Model 40A, GGB Industries Inc., USA). The resonance frequency and magnitude of the conductance peak are determined from the device conductance obtained from the measured S_{11} parameter. The EIS port is connected to a potentiostat (SP-300 with Ultra Low Current adapter by Bio-Logic Science Instruments, France). The impedance spectra of the sensor were obtained by applying a 7.07 mV RMS AC voltage in the frequency range from 1 Hz to 1 MHz. Each data point was averaged 10 times.

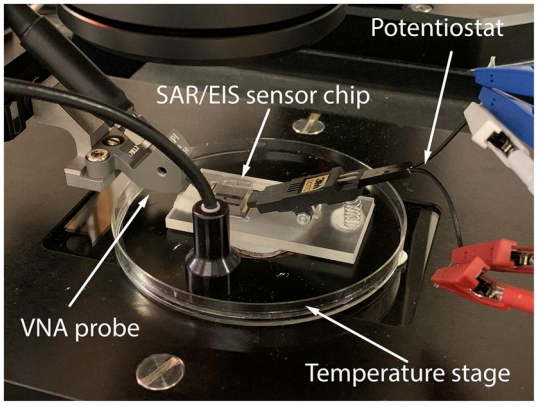

Fig. 4. Photograph of the measurement setup used for the sensor characterisation. The sensor chip is placed under the microscope on a temperature-controlled stage in a holder that hosts the necessary EIS wiring and spring-loaded contacts. On the left side, the chip is contacted with a VNA probe for SAR response detection.

3. Impedance spectroscopy fundamentals and equivalent circuit model

Impedimetric measurement data need to be quantified through a lumped element model to obtain characteristic quantities. Suitable equivalent models with a good fit to real measurements were previously proposed[45–49].

Fig. 5 shows a schematic representation of the IDE structure in contact with the solution and the deposited (lipid) film, and its simplified electrical equivalent circuit model (ECM) giving the best fit. R_{Sol} represents the intrinsic buffer solution resistance, superimposed upon

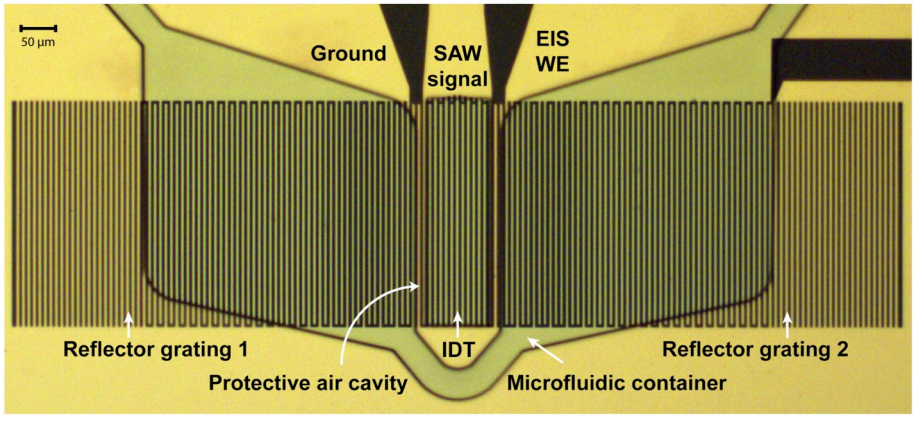

Fig. 3. Optical microscopy image (top view) of the assembled microfluidic SAR/EIS tandem sensor.

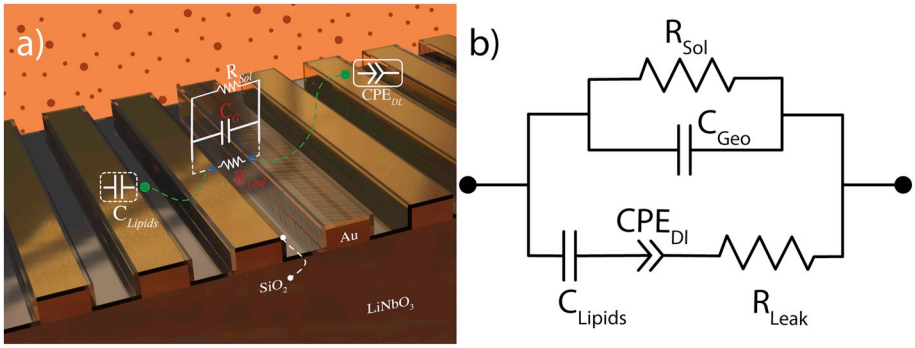

Fig. 5. The IDE equivalent circuit a) sketch view b) Modified Randle's cell model.

the parasitic resistance of the IDE structure itself. The latter is the only contribution when measuring in air (R_{Geo}), R_{Leak} is determined by the leakage current passing through the electrode interface with the analyte and the biochemical deposits, and C_{Geo} is a geometric (stray) capacitance between two electrodes through the medium (including the $LiNbO_3$ substrate, the liquid dielectric permittivity and the thin SiO_2 coating, as well as any parasitic capacitances in parallel emanating from the connection of the IDEs to the potentiostat). The capacitance of the lipid layer C_{Lipids} is in series with the double layer capacitance C_{Dl} formed between the IDEs and the analyte. In reality, the double-layer capacitor often deviates from an ideal capacitor due to roughness, porosity and inhomogeneities on the IDE surfaces. For that reason, an empirically modelled constant phase impedance element (CPE) is used instead of an ideal capacitor to represent C_{Dl}. In our system, the presence of a sputtered (porous) SiO_2 thin film over the Au IDEs justifies the use of CPE in the model. The electrical double layer capacitance mainly depends on the ion type and concentration, while changes in CPE_{Dl} are also attributed to the formation of an additional deposited layer on the electrode surface, which in our case is a lipid layer. In air this equivalent circuit is simplified, featuring only the upper branch of capacitance and parasitic resistance in parallel. When the lipids are not present on the sensing surface, the CPE-complementary C_{Lipids} is also omitted from the in-liquid model.

In practical EIS sensing experiments the sensitivity is considered with regard to the change of the lumped elements. Most sensitive elements are identified and selected as sensing quantities. Although the lumped elements have physical meaning, their behaviour is typically not independently determined because of the inherent complexity of the sample composition. Often CPE_{Dl} and R_{Leak} components are good identifiers of interface phenomena resulting from biochemical reactions, while C_{Geo} and R_{Sol} provide information for the bulk environment.

3.1. EIS-SAR sensor characterisation

3.1.1. In air and DI water

The baseline performance of the EIS-SAR sensor was initially assessed through measurements in air and deionized water (DIW). The high frequency response is characterized with a well-defined high quality-factor resonance at about 185 MHz, even when the device is immersed in DIW Fig. 6.

Upon exposure to DIW, a strong response of the SAW resonance frequency of about −2000 ppm and the magnitude of conductance peak of about −32% are observed, which is in agreement with our previous measurements [34]. Impedimetric measurements in air and DIW reveal the distinct performances of the IDE in both environments. As seen from the Nyquist plot in Fig. 7a, the IDE performance in air is well represented by the semi-circle determined by the stray capacitance C_{Geo} = 19.3 pF, and the parasitic resistance of about 1.7 GΩ. At frequencies below 10 Hz the measurement instability is dominating, which is a known issue in EIS at very high impedances, since very small

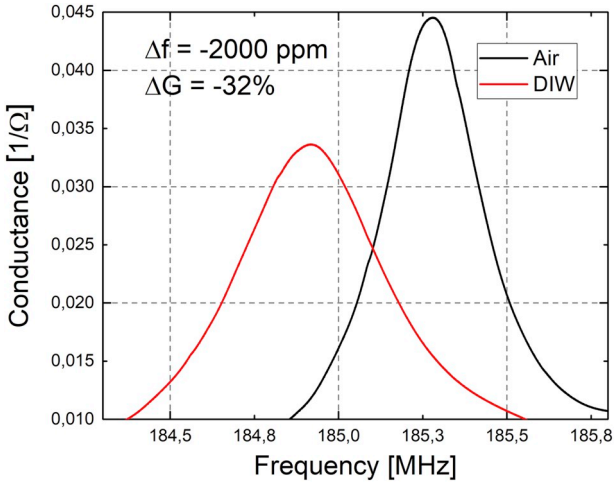

Fig. 6. Close-in resonance conductance of the fabricated EIS-SAR sensor. The black curve represents the measurement in air-filled, and the red curve in water-filled microfluidic containers. (For interpretation of the references to colour in this figure legend, the reader is referred to the web version of this article.)

currents are being measured. Upon contact with DIW the constant phase element becomes evident in the Nyquist plot (Fig. 7b) through the constant slope of the curve, especially in the frequency range below 1 kHz. In the frequency range from 1 kHz to 1 MHz a semicircle can be seen, the diameter of which depends on the conductance of the media and the stray capacitance C_{Geo} in parallel. At frequencies below 1 kHz the impedance is dominated by CPE_{Dl}, which is caused by the electrical double-layer at the IDE/DIW interface.

Considering the noise-related signal instability at frequencies below 10 Hz, the impedance curve recorded at 10–100 Hz appears to be appropriate for monitoring the change of CPE_{Dl}. At higher frequencies up to 1 MHz, the dielectric behaviour (i.e. C_{Geo}) of the solution dominates the signal.

The IDE capacitance shifted to C_{Geo} = 65.4 pF, which accounts well for the twice larger dielectric permittivity of DIW as compared to $LiNbO_3$. R_{Sol} has shifted down to 0.9 GΩ due to the finite resistivity of the DIW. The appearance of double-layer is manifested by the CPE_{Dl} = 1.2 nF/(s^n cm^2) and interface leakage current determined by the R_{Leak} = 47 MΩ. Although the EIS response is dominated by the latter, in the higher frequency range the stray capacitance becomes a current flow path concurrent to the DIW/IDE interface.

The integrated EIS-SAR sensor clearly demonstrates physically meaningful responses, being able to provide complementary data for the acoustic and electric properties at the sensor surface. Furthermore, the dominating role of the CPE in the impedimetric spectra suggests enhanced EIS sensitivity towards physicochemical processes at the sensing surface.

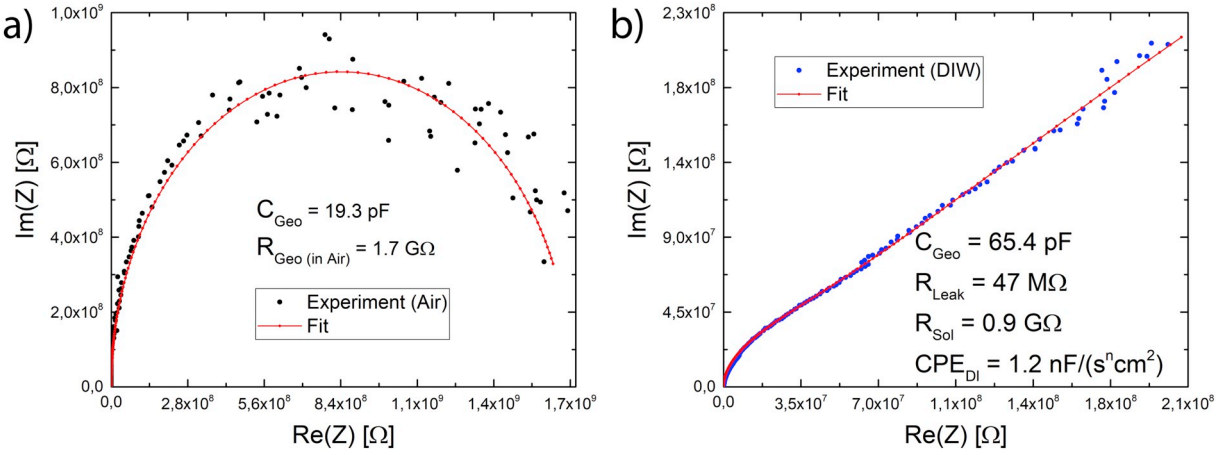

Fig. 7. Nyquist plot of the EIS response for data obtained experimentally and their fit, along with extracted values for each equivalent circuit model component, shown for a) air and b) DIW.

4. Sensing of lipid deposition

Initially, DIW was replaced with HEPES buffer needed for the subsequent lipid deposition. As seen from Table 1, this is accompanied by an additional SAW resonance frequency shift of about −118 ppm, along with a 2.1% decrease of the conductance peak magnitude. The impedimetric measurement shows an overall decrease of impedance as seen on the Bode plot in Fig. 8. The decrease is seen both in lower and higher frequency regions suggesting changes both near the IDE surface and in the liquid volume. This observation is further quantified in Table 1, where CPE_{Dl} increases 30% from 1.2 nF/(s^n cm^2) to 1.6 nF/(s^n cm^2).

The lipid membrane was formed in the first step by exposing the SiO_2-coated surface to a multilamellar lipid vesicle (MLV) suspension in HEPES buffer [50]. A detailed description of MLV suspension preparation routines can be found in the materials and methods section below. The SAW resonance (see Table 1) underwent a strong downshift of −86 ppm due to the viscoelastic mass loading at the surface, while the magnitude of peak conductance decreased by 2.3%, caused by acoustic wave damping in the lipid layer. The values were recorded after 10 min, when we observed saturation of the signal and flushed away the excess MLVs. Regarding the EIS response, the deposition of lipid bilayer on the sensor surface adds a new charged layer as a leaky capacitor in series with the double layer, but is also causing improved conduction through the double layer, i.e., a change in the fundamental double-layer properties. These effects are clearly manifested below 1 kHz, where the impedance is lower as compared to HEPES. For frequencies above 1 kHz, the changes are insignificant since the response there is dominated by the electrical properties of HEPES. These observations are further confirmed by extracting the elements of the ECM through a fitting process (see Table 1). Furthermore, we observed an increase of CPE_{Dl} by 45%, and the reduction of R_{Leak} by 31%. A complementary capacitance C_{Lipids} = 3.2 nF was extracted from the fit. Together, the SAW and EIS quantities suggest that a layer with distinct viscoelastic properties, and leaky capacitance behaviour has been formed on the sensing surface.

Upon addition of Ca^{2+} ions, a strong upshift of both the SAW resonance frequency and magnitude of peak conductance by about +19 ppm and +2.1%, respectively, was determined. This shift brought the response to levels of the magnitude of peak conductance very close to the HEPES level, while the resonant frequency remained closer to the lipid levels. The measurement was performed after the transformation was complete, which was confirmed by the stabilized sensor response. This response to Ca^{2+}-induced lipid spreading is in good agreement with previously published data [35]. A relatively strong upshift of the magnitude of the peak conductance in the range between 2%–3%, and an upshift in the frequency around +20 ppm were observed.

In our previous work [35] we provided an explanation of this behaviour in relation to the improved rigidity upon Ca^{2+}-induced formation of surface-supported molecular lipid films followed by

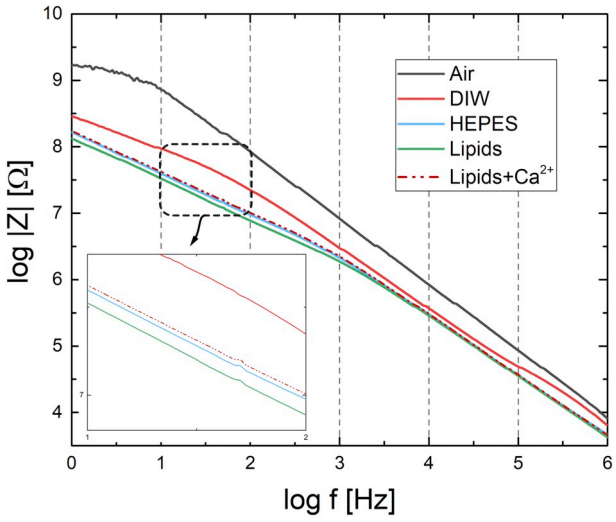

Fig. 8. Bode plot of impedance spectra for different analytes. An inset in the bottom left corner is a zoomed-in region of 10 Hz–100 Hz response from the same plot. The slightly increased signal at 50 Hz is an artefact originating from the 220 V/50 Hz power grid, it appears in all recordings in our setup.

Table 1
Extracted EIS-SAW sensing quantities: SAW resonance frequency shifts [Δf], SAW conductance peak magnitude shifts [ΔG], EIS stray capacitance C_{Geo}, EIS interface leak resistor R_{Leak}, EIS double layer constant phase element CPE_{Dl}.

Parameter:	Δf [ppm]	ΔG [%]	C_{Geo} [pF]	R_{Leak} [MΩ]	CPE_{Dl} [nF/(s^n cm^2)]
DIW to HEPES	−118	−2.1%	65.4	47–4.2 (−91%)	1.2–1.6 (+30%)
HEPES to lipids	−86	−2.3%	65.8	4.2–2.9 (−31%)	1.6–2.9 (+45%)
Addition of Ca^{2+}	+19	+2.1%	65.7	2.9–3.3 (+14%)	2.9–1.8 (−38%)

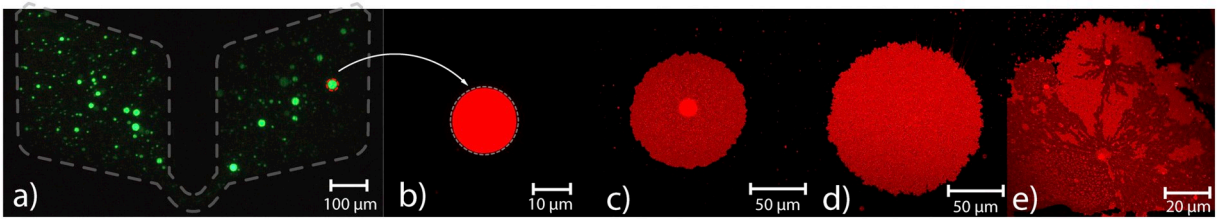

Fig. 9. Fluorescent micrographs of a) MLVs deposited on the sensor surface – the shape of the two fluidic chambers is outlined with a dashed contour; b) Individual spherical lipid reservoir (MLV) containing multiple stacked layers of lipid membranes (onion shell vesicle). The MLV in (b) is structurally representative of, but not identical to, the vesicle encircled in (a); c) Double lipid bilayer membrane formed by self-spreading from the MLV (bright spot at the center) upon addition of Ca^{2+} to the ambient buffer; d) Lipid membrane after removal of excess lipid reservoirs due to an applied hydrodynamic flow; e) Continuing spreading causes an increase in membrane tension, eventually resulting in rupturing of the upper bilayer membrane.

rupturing, and the occurrence of nano-tubular protrusions floating in the aqueous media [51–53]. For reference, we have captured this behaviour by laser scanning confocal microscopy, both on the sensor surface (Fig. 9a), and on a SiO_2-coated glass surface (Fig. 9 b–e). In Fig. 9a, a mixed film of lipid layer (lower intensity dark green) and sparse MLVs (the lighter-larger objects having a size of about 10 µm and larger) are seen attached to the SiO_2-coated sensor surface. In a separate experiment an MLV (Fig. 9b) on SiO_2-coated transparent glass substrate, allowing for close-proximity observations, was subjected to Ca^{2+} interaction. Calcium ions at concentrations > 0.8 mM initiate tension-driven surface wetting (Marangoni flow) by the lipid deposit, where the lipid layer spreads in a circular fashion as a rolling double bilayer from the MLV, gradually consuming the MLV (Fig. 9c) [54]. Excess MLVs are flushed away in a subsequent washing step (Fig. 9d), leaving behind a continuous lipid film on the surface. The membranes originating from different spreading patches merge in this process (Fig. 9e). Ca^{2+} ions continuously pin the lipid layer to the surface, forming a rigidified solid-supported layer. When the lipid reservoirs are depleted, the continuous adhesion to the surface promoted by Ca^{2+} pinning causes a significant increase in lipid membrane tension, eventually resulting in rupturing. The lipid material released by the rupture process is transferred onto the proximal bilayer [50,52].

Detailed information on the Ca^{2+}-induced changes has been extracted through simultaneous EIS characterisation. The Bode plot in Fig. 8 shows that the magnitude of impedance has recovered slightly above the HEPES level, which is associated with a significantly decreased conductivity at the interface layer, suggesting an interface structure with reduced CPE_{Dl} and/or increased R_{Leak}. This behaviour appears to result from the formation of an extensively ruptured rigid layer, which on one side reduces the capacitance of the layer while on the other reduces the surface leak conductivity by neutralisation of charge carriers through the Ca^{2+} reaction. As shown in Table 1, CPE_{Dl} has decreased by 38%, while R_{Leak} increased by 14%. Moreover, C_{Lipid} practically vanished, further supporting our notion on the electrical characteristics of the ruptured surface. Both the acoustic and the EIS responses underwent extensive signal recovery towards the base HEPES levels. The SAW resonance frequency and R_{Leak} have shown a moderate recovery, which is due to the partial, but not complete removal of weakly adhered reservoir vesicles. The remaining MLVs are transformed into the double bilayer during the spreading process. The magnitude of peak conductance, and CPE_{Dl} recovered almost to the levels of HEPES, which we attribute to the loss of a homogeneous lipid double bilayer in the rupturing process.

5. Materials and methods for the lipid assay

5.1. Chemicals

Soybean Polar Lipid Extract (SPE) purchased from Avanti Polar Lipids, Inc. (USA). Chloroform and 4-(2- hydroxyethyl), PBS tablets, and piperazine-1-ethanesulfonic acid (HEPES) solution (1 M) were obtained from Sigma-Aldrich (Missouri, USA). Calcium chloride ($CaCl_2$) was purchased from KEBO lab (Sweden). Two different fluorophore-conjugated lipids were used for labelling. 2-Dioleoyl-sn-glycero- 3-phosphoethanolamine with the fluorophore ATTO-488 (ATTO488 - DOPE) [Fig. 9a] was purchased from ATTO-TEC (Germany) and the 1,2-dipalmitoyl-sn-glycero-3-phosphoethanolamine-N-(lissamine rhodamine B sulfonyl) (ammonium salt) (16:0 Liss Rhod PE) was purchased from Avanti Polar Lipids [Fig. 9b–e].

6. Vesicle preparation

The multilamellar lipid vesicles were composed of SPE, consisting of PE (phosphatidylethanolamine) 22.1%, PI 18.4%, PC 45.7%, PA 6.9%, and other lipids 6.9%. The lipid mixtures in the fluorescent micrographs contained fluorescently labelled lipid ATTO488-DOPE (1 wt%) or Rhodamine-PE (1 wt%). The giant vesicles were prepared as described in [55] and stored in 0.5 mL Eppendorf tubes at −20 °C until use.

A glass coverslip (Menzel Gläzer 24 × 60) with 100 nm surface coating of SiO_2 was prepared by reactive sputtering. A PDMS ring was placed on top of the surface, and 500 µL 10 mM HEPES buffer (pH 7.4) was placed inside the PDMS ring. An addition of 60 µL of the giant lipid vesicle suspension was placed inside the HEPES buffer solution for 10 min. Thereafter, the HEPES buffer was exchanged for a solution of $CaCl_2$ solution with the concentration 5 mM. After 10 min, the solution was exchanged again with HEPES buffer and imaged.

Stereo-fluorescence microscopy: A Leica M205 FA upright fluorescence stereo microscope, equipped with a 1× 'Planachromat' main objective, an external halogen light source, and the GFP and DSR filter sets, was used for obtaining Fig. 9a.

Microscopy: A confocal laser scanning microscopy system (Leica SP8, Germany), with HCX PL APO CS 40× oil objective (NA: 1.25) was used for acquisition of confocal fluorescence images (Fig. 9 b–e). The excitation wavelength for the imaging of the Rhodamine-PE was provided via a white-light laser source (Leica) at 560 nm and the emission was collected at 583 nm using a hybrid fluorescence filter.

7. Conclusions

Operation of a combined surface acoustic resonance and impedimetric sensor within the confines of a single sensor die was demonstrated. The sensor was designed in a tandem arrangement, in which both sensing circuits physically share surfaceprinted components, in this case interdigital electrode fingers, but are operated in different frequency ranges through two electrical interface ports. The proposed integration SAR-EIS scheme demonstrates crosstalk below −60 dB, and enhanced sensitivities towards particle and molecular film deposits at the sensing surface, and their calcium ion-induced transformation into each other. The obtained multiparametric sensor response was discussed with respect to the expected and observed phenomena, providing a first impression of the rich information that can be acquired by a tandem sensor. The SAW and the EIS responses are not only

complementary in view of detecting the nature of the molecular layer structures and their properties, but also provided insights into possibilities for further improvement of the sensor figures of merit.

Declaration of completing interest

The authors declare no conflict of interest

Acknowledgements

We thank Gizem Karabiyik from the University of Oslo for providing the Ca^{2+} induced lipid spreading and rupturing experiments. This work was made possible through financial support obtained from the Swedish Research Council (Vetenskapsrådet) Project Grant 2015-04561, the H2020 ITN "Chemical Reaction Networks – CReaNET" - Ref. 812868, the Research Council of Norway (Forskningsrådet) Project Grant 274433, Swedish Foundation for Strategic Research (SSF) (GMT14-0077), UiO: Life Sciences Convergence Environment as well as the start-up funding provided by the Centre for Molecular Medicine Norway & Faculty of Mathematics and Natural Sciences at the University of Oslo.

References

[1] G. Luka, A. Ahmadi, H. Najjaran, E. Alocilja, M. DeRosa, K. Wolthers, et al., Microfluidics integrated biosensors: a leading technology towards lab-on-a-chip and sensing applications, Sensors. (Basel) 15 (2015) 30011–30031.
[2] Y.S. Zhang, J. Aleman, S.R. Shin, T. Kilic, D. Kim, S.A.M. Shaegh, et al., Multisensor-integrated organs-on-chips platform for automated and continual in situ monitoring of organoid behaviors, Proc. Natl. Acad. Sci. U. S. A. 114 (2017) E2293–E2302.
[3] S.S. Chen, M.H. Shamsi, Biosensors-on-chip: a topical review, J. Micromech. Microeng. 27 (2017).
[4] K. Lange, B.E. Rapp, M. Rapp, Surface acoustic wave biosensors: a review, Anal. Bioanal. Chem. 391 (2008) 1509–1519.
[5] Y.Q. Fu, J.K. Luo, X.Y. Du, A.J. Flewitt, Y. Li, G.H. Markx, et al., Recent developments on ZnO films for acoustic wave based bio-sensing and microfluidic applications: a review, Sensors. and.Actuators B-Chem 143 (2010) 606–619.
[6] Y.Q. Fu, J.K. Luo, N.T. Nguyen, A.J. Walton, A.J. Flewitt, X.T. Zu, et al., Advances in piezoelectric thin films for acoustic biosensors, acoustofluidics and lab-on-chip applications, Prog. Mater. Sci. 89 (2017) 31–91.
[7] D. Grieshaber, R. MacKenzie, J. Voros, E. Reimhult, Electrochemical biosensors - sensor principles and architectures, Sensors 8 (2008) 1400–1458.
[8] D.B. Go, M.Z. Atashbar, Z. Ramshani, H.-C. Chang, Surface acoustic wave devices for chemical sensing and microfluidics: a review and perspective, Anal. Methods 9 (2017) 4112–4134.
[9] X. Ding, P. Li, S.-C.S. Lin, Z.S. Stratton, N. Nama, F. Guo, et al., Surface acoustic wave microfluidics, Lab Chip 13 (2013) 3626–3649.
[10] F. Liu, A.N. Nordin, F. Li, I. Voiculescu, A lab-on-chip cell-based biosensor for label-free sensing of water toxicants, Lab Chip 14 (2014) 1270–1280.
[11] E. Briand, M. Zach, S. Svedhem, B. Kasemo, S. Petronis, Combined QCM-D and EIS study of supported lipid bilayer formation and interaction with pore-forming peptides, Analyst 135 (2010) 343–350.
[12] A. Sabot, S. Krause, Simultaneous quartz crystal microbalance impedance and electrochemical impedance measurements. Investigation into the degradation of thin polymer films, Anal. Chem. 74 (2002) 3304–3311.
[13] Q.J. Xie, C.H. Xiang, X.H. Yang, Y.Y. Zhang, M. Li, S.Z. Ya, Simultaneous impedance measurements of two one-face sealed resonating piezoelectric quartz crystals for in situ monitoring of electrochemical processes and solution properties, Anal. Chim. Acta 533 (2005) 213–224.
[14] H. He, Q.J. Xie, Y.Y. Zhang, S.Z. Yao, A simultaneous electrochemical impedance and quartz crystal microbalance study on antihuman immunoglobulin G adsorption and human immunogloulin G reaction, J. Biochem. Biophys. Methods 62 (2005) 191–205.
[15] E.M. Pinto, D.M. Soares, C.M.A. Brett, Interaction of BSA protein with copper evaluated by electrochemical impedance spectroscopy and quartz crystal microbalance, Electrochim. Acta 53 (2008) 7460–7466.
[16] A. Janshoff, J. Wegener, M. Sieber, H.J. Galla, Double-mode impedance analysis of epithelial cell monolayers cultured on shear wave resonators, Eur. Biophys. J. Biophys. Lett. 25 (1996) 93–103.
[17] A.V. Mamishev, K. Sundara-Rajan, F. Yang, Y.Q. Du, M. Zahn, Interdigital sensors and transducers, Proc. IEEE 92 (2004) 808–845.
[18] Z. Rácz, M. Cole, J.W. Gardner, S. Pathak, M.D. Jordan, R.A.J. Challiss, Cell-based surface acoustic wave resonant microsensor for biomolecular agent detection, 2011 16th International Solid-State Sensors, Actuators and Microsystems Conference2011pp. 2168–2171.
[19] Y.C. Xu, X.W. Xie, Y. Duan, L. Wang, Z. Cheng, J. Cheng, A review of impedance measurements of whole cells, Biosens. Bioelectron. 77 (2016) 824–836.
[20] I. Katardjiev, V. Yantchev, Recent developments in thin film electro-acoustic technology for biosensor applications, Vacuum 86 (2012) 520–531.
[21] M. DeMiguel-Ramos, B. Diaz-Duran, J.M. Escolano, M. Barba, T. Mirea, J. Olivares, et al., Gravimetric biosensor based on a 1.3 GHz AlN shear-mode solidly mounted resonator, Sensors. And. Actuators B-Chem 239 (2017) 1282–1288.
[22] M. Nirschl, A. Rantala, K. Tukkiniemi, S. Auer, A.C. Hellgren, D. Pitzer, et al., CMOS-integrated film bulk acoustic resonators for label-free biosensing, Sensors 10 (2010) 4180–4193.
[23] R. Hoffmann, M. Schreiter, J. Heitmann, The concept of thin film bulk acoustic resonators as selective CO2 gas sensors, J. Sens. Sensor. Syst. 6 (2017) 87–96.
[24] T. Mirea, V. Yantchev, Influence of liquid properties on the performance of S-0-mode lamb wave sensors: a theoretical analysis, Sensors. And. Actuators. B-Chem 208 (2015) 212–219.
[25] T. Mirea, V. Yantchev, J. Olivares, E. Iborra, Influence of liquid properties on the performance of S-0-mode lamb wave sensors II: experimental validation, Sensors. And. Actuators. B-Chem 229 (2016) 331–337.
[26] C. Caliendo, M. Hamidullah, Guided acoustic wave sensors for liquid environments, J. Phys. D-Appl. Phys 52 (2019).
[27] S. Hohmann, S. Kogel, Y. Brunner, B. Schmieg, C. Ewald, F. Kirschhofer, et al., Surface acoustic wave (SAW) resonators for monitoring conditioning film formation, Sensors. (Basel) 15 (2015) 11873–11888.
[28] T. Nomura, A. Saitoh, Y. Horikoshi, Measurement of acoustic properties of liquid using liquid flow SH-SAW sensor system, Sensors Actuators. B-Chem. 76 (2001) 69–73.
[29] A. Mujahid, F.L. Dickert, Surface acoustic wave (SAW) for chemical sensing applications of recognition layers, Sensors. (Basel) 17 (2017).
[30] Z. Ramshani, A.S.G. Reddy, B.B. Narakathu, J.T. Wabeke, S.O. Obare, M.Z. Atashbar, SH-SAW sensor based microfluidic system for the detection of heavy metal compounds in liquid environments, Sensors Actuators B-Chem. 217 (2015) 72–77.
[31] M. Agostini, G. Greco, M. Cecchini, A Rayleigh surface acoustic wave (R-SAW) resonator biosensor based on positive and negative reflectors with sub-nanomolar limit of detection, Sensors Actuators B-Chem. 254 (2018) 1–7.
[32] V.H. Nguyen, C. Kaulen, U. Simon, U. Schnakenberg, Single interdigital transducer approach for gravimetrical SAW sensor applications in liquid environments, Sensors 17 (2017) 13.
[33] K. Kustanovich, V. Yantchev, A. Jesorka, IEEE, Design and Characterization of Surface Acoustic Wave Resonance (SAR) System for in-Liquid Sensing, 2017 Joint Conference of the European Frequency and Time Forum and IEEE International Frequency Control Symposium, (2017), pp. 652–655.
[34] K. Kustanovich, V. Yantchev, V. Kirejev, G.D.M. Jeffries, T. Lobovkina, A. Jesorka, A high-performance lab-on-a-chip liquid sensor employing surface acoustic wave resonance, J. Micromech. Microeng. 27 (2017) 9.
[35] K. Kustanovich, V. Yantchev, A. Olivefors, B.A. Doosti, T. Lobovkina, A. Jesorka, A high-performance lab-on-a-chip liquid sensor employing surface acoustic wave resonance: part II, J. Micromech. Microeng. 29 (2019) 8.
[36] G. Denisov, S. Wanaski, P. Luan, M. Glaser, S. McLaughlin, Binding of basic peptides to membranes produces lateral domains enriched in the acidic lipids phosphatidylserine and phosphatidylinositol 4,5-bisphosphate: an electrostatic model and experimental results, Biophys. J. 74 (1998) 731–744.
[37] D. Martin, Nanobiotechnology of Biomimetic Membranes, Springer US, 2007.
[38] K.Y. Hashimoto, Surface Acoustic Wave Devices in Telecommunications: Modelling and Simulation, Springer Berlin Heidelberg, 2013.
[39] H. Shimizu, Y. Suzuki, T. Kanda, Love-Type-Saw Resonator of Small Size with Very Low Capacitance Ratio and its Application toVCO, (1990).
[40] M. Kadota, S. Tanaka, Wideband acoustic wave resonators composed of hetero acoustic layer structure, Jpn. J. Appl. Phys. 57 (2018).
[41] D. Morgan, Surface Acoustic Wave Filters: With Applications to Electronic Communications and Signal Processing, Elsevier Science, 2010.
[42] F. Lisdat, D. Schafer, The use of electrochemical impedance spectroscopy for biosensing, Anal. Bioanal. Chem. 391 (2008) 1555–1567.
[43] Y.N. Xia, G.M. Whitesides, Soft lithography, Annu. Rev. Mater. Sci. 28 (1998) 153–184.
[44] G.M. Whitesides, E. Ostuni, S. Takayama, X.Y. Jiang, D.E. Ingber, Soft lithography in biology and biochemistry, Annu. Rev. Biomed. Eng. 3 (2001) 335–373.
[45] P. Van Gerwen, W. Laureyn, W. Laureys, G. Huyberechts, M.O. De Beeck, K. Baert, et al., Nanoscaled interdigitated electrode arrays for biochemical sensors, Sensors Actuators B-Chem. 49 (1998) 73–80.
[46] E. Valera, J. Ramon-Azcon, A. Rodriguez, L.M. Castaner, F.J. Sanchez, M.P. Marco, Impedimetric immunosensor for atrazine detection using interdigitated mu-electrodes (ID mu E's), Sensors Actuators B-Chem. 125 (2007) 526–537.
[47] Z.W. Zou, J.H. Kai, M.J. Rust, J. Han, C.H. Ahn, Functionalized nano interdigitated electrodes arrays on polymer with integrated microfluidics for direct bio-affinity sensing using impedimetric measurement, Sensors Actuators A-Phys. 136 (2007) 518–526.
[48] S. Rana, R.H. Page, C.J. McNeil, Impedance spectra analysis to characterize interdigitated electrodes as electrochemical sensors, Electrochim. Acta 56 (2011) 8559–8563.
[49] L. Wang, M. Veselinovic, L. Yang, B.J. Geiss, D.S. Dandy, T. Chen, A sensitive DNA capacitive biosensor using interdigitated electrodes, Biosens. Bioelectron. 87 (2017) 646–653.
[50] I. Gozen, P. Dommersnes, I. Czolkos, A. Jesorka, T. Lobovkina, O. Orwar, Fractal avalanche ruptures in biological membranes, Nat. Mater. 9 (2010) 908–912.
[51] B.A. Doosti, W. Pezeshkian, D.S. Bruhn, J.H. Ipsen, H. Khandelia, G.D.M. Jeffries, et al., Membrane tubulation in lipid vesicles triggered by the local application of calcium ions, Langmuir 33 (2017) 11010–11017.
[52] I. Gozen, C. Billerit, P. Dommersnes, A. Jesorka, O. Orwar, Calcium-ion-controlled nanoparticle-induced tubulation in supported flat phospholipid vesicles, Soft Matter 7 (2011) 9706–9713.
[53] A. Melcrova, S. Pokorna, S. Pullanchery, M. Kohagen, P. Jurkiewicz, M. Hof, et al., The complex nature of calcium cation interactions with phospholipid bilayers, Sci. Rep. 6 (2016).
[54] A. Ainla, I. Gozen, O. Orwar, A. Jesorka, A microfluidic diluter based on pulse width flow modulation, Anal. Chem. 81 (2009) 5549–5556.
[55] B.A. Doosti, A.S. Cans, G.D.M. Jeffries, T. Lobovkina, Membrane remodeling of giant vesicles in response to localized calcium ion gradients, Jove-J. Visualized Exp. 137 (2018) 1–9. Art. No. e57789.